In situ study on fracture behaviour of white etching layers formed on rails

Kumar, Ankit; Saxena, A. K.; Kirchlechner, C.; Herbig, M.; Brinkmann, S.; Petrov, R. H.; Sietsma, J.

DOI
10.1016/j.actamat.2019.08.060

Publication date
2019

Document Version
Accepted author manuscript

Published in
Acta Materialia

In situ study on fracture behaviour of white etching layers formed on rails

A. Kumar[a,b*], A. K. Saxena[b], C. Kirchlechner[b*], M. Herbig[b*], S.Brinkmann[b], R.H.Petrov[a,c], J. Sietsma[a,c]

[a] Delft University of Technology, Department of Materials Science and Engineering, Mekelweg 2, 2628CD Delft, The Netherlands

[b] Max-Planck-Institut für Eisenforschung GmbH, Max-Planck-Str. 1, 40237 Düsseldorf, Germany

[c] Ghent University, Department of Electrical Energy, Metals, Mechanical Constructions & Systems, Technologiepark 903 Ghent, Belgium

[*] Correspondence to – A.Kumar-2@tudelft.nl, kirchlechner@mpie.de, and m.herbig@mpie.de

Abstract

Failure in engineering materials like steels is strongly affected by in-service deleterious alterations in their microstructure. White Etching Layers (WELs) are an example of such in-service alterations in the pearlitic microstructure at the rail surface. Cracks initiate in the rails due to delamination and fracture of these layers and propagate into the base material posing severe safety concerns. In this study, we investigate the microscale fracture behaviour of these WELs. We use *in situ* elastic-plastic fracture mechanics using *J*-integral to quantify the fracture toughness. Although usually assumed brittle, the fracture toughness of 21 – 25 MPa√m reveals a semi-brittle nature of WELs. Based on a comparison of the fracture toughness and critical defect size of WELs with the undeformed pearlitic steels, WELs are detrimental for rails. In the micro fracture tests, WELs show crack tip blunting, branching, and significant plasticity during crack growth due to their complex microstructure. The fracture behaviour of the WELs is governed by their microstructural constituents such as phases (martensite/austenite), grain size, dislocation density and carbon segregation to dislocations and grain boundaries. We observed dislocation annihilation in some martensitic grains in the WELs which also contributes to their fracture behaviour. Additionally, the strain-induced transformation from austenite to martensite affects the crack growth and fracture.

Keywords- White Etching Layer (WEL), Elastic-Plastic Fracture Mechanics (EPFM), Elastic-plastic conditional fracture toughness ($K_{IQ,J}$), Electron Backscatter Diffraction (EBSD), Transmission Electron Microscopy (TEM) and Atom Probe Tomography (APT), Martensite, Austenite, Grain size and Kernel Average Misorientation (KAM).

1. Introduction

The design of sustainable new materials with well-controlled structural integrity requires a macro- to microscale understanding of degradation and failure of the conventional materials. Steels are one of the most commonly used conventional materials around the world. The study of failure in steels is crucial to ensure the safety in engineering applications such as construction, transport, energy, *etc*. In the transport industry, railway consists of 1,370,782 km length of rail track worldwide [1] and this length is still growing. In this entire rail network, the pearlitic steels are the most commonly used steels [2]. Failure in pearlitic railway steels is strongly affected by the detrimental microstructural changes on the rail raceway due to the wheel-rail contact. Conventional pearlitic steels are prone to the formation of White Etching Layers (WELs) on the rail raceway during the wheel-rail interaction [3–11]. Delamination and partial brittle fracture of these WELs cause micro-crack initiation in the rails [4,5,9,10,12–14]. These micro-cracks grow into the base material and this propagation finally leads to rail track failure, posing a safety threat to the passengers. Worldwide, the rail industries invest tens of million dollars per year to grind various in-service surface defects and to remove the WELs before extended cracks form [15,16].

In the literature, two hypotheses are proposed for the formation mechanism of the WELs. The first hypothesis suggests that the WELs form only due to severe plastic deformation during wheel-rail contact and stress assisted cementite dissolution leads to the formation of nano-crystalline ferrite in the WEL microstructure [10,11,13]. The second hypothesis suggests that WELs form due to the temperature rise above austenite start temperature – followed by fast cooling [3,5,9]. This temperature variation leads to the formation of martensite and austenite. However, recent insights have shown that WELs form by the combination of the temperature rise above the austenite start temperature and the plastic deformation at the rail raceway [17–19]. Still, there is considerable debate among the research community concerning the WEL formation mechanism. Typically, the WELs consist of complex microstructural features such as martensite, retained austenite and partially dissolved parent cementite [7,17–19]. In addition, the overall microstructural evolution varies in different studies because of the variation in rail-wheel contact conditions such as wheel profile, axle load, train speed and slip rate. In spite of having a detailed understanding on formation mechanism and microstructural evolution of the WELs, there is no detailed study available in literature, which focuses on the fracture behaviour of the WEL on microstructural scale. Most of the available studies only focus on macro scale fracture due to the WELs in rails [4,20].

The WELs are considered to be among the metallurgical causes for crack initiation and propagation in rails because of their brittle nature [4,5,9,14,18,19]. However to date, there is no quantification of the fracture toughness of WELs and their fracture behaviour has not been studied in detail. This lack of fracture properties is primarily due to the small size of in-service WELs. The fracture behaviour of such small features cannot be determined via conventional testing. Only small scale *in situ* fracture mechanics allow studying the fracture behaviour of these microscale features. Micromechanics also allows analysing special microstructural features such as single crystals, grain boundaries, phase boundaries, coatings and multilayer microscale systems [21–28].

In the present study, we show *in situ* microscale fracture experiments on the WELs. The fracture toughness values of the WELs can be of utmost importance for modelling the failure in rails due to the presence of WELs at the rail surface. They can also enable the estimation of quantities such as critical WEL thickness in rails and consequently the required grinding intervals in rails to avoid failure and also to minimize the grinding costs. For brittle materials, microscale fracture experiments use notched micro-cantilevers and apply Linear Elastic Fracture Mechanics (LEFM) [21,22,32,23–26,28–31] to quantify the fracture toughness. In these conditions, the size of the plastic zone at the crack tip should be significantly smaller than the specimen dimensions [33]. Thus, the LEFM approach is useful primarily for brittle materials, which fracture without any plastic deformation. Application of LEFM for ductile and semi-brittle materials will lead to the underestimation of the fracture toughness. We use both the LEFM and Elastic-Plastic Fracture Mechanics (EPFM) approach [33,34] to calculate the fracture toughness of the WELs.

In this study, the fracture toughness of the WELs is compared with those of undeformed pearlite, quenched martensite (same chemical composition as pearlitic steels in this work), heavily drawn nanocrystalline pearlite, iron (Fe) and nanocrystalline Fe thin films in order to put the quantified fracture behaviour of the WELs into context. We discuss the effect of microstructural features such as the presence of austenite, grain size, dislocation density and carbon (C) segregation at the dislocations and the grain boundaries in the WELs on the fracture response. Additionally, we investigate the strain-induced transformation of austenite to martensite during crack growth in the WELs.

2. Materials and experimental methods

The specimens containing WEL were cut from an in-service curved rail track with 400 m radius. The approximate load passage was 200 Mt with an axial load ranging from 120 to 180 kN [19]. The chemical composition of the studied R350HT steel is Fe-0.72C-1.1Mn-0.56Si-0.11Cr (wt.%), or Fe-3.25C-1.09Si-1.1Mn-0.11Cr (at.%). These steels were produced by 6 pass hot rolling at 1000 °C into the form of a rail, followed by annealing at 900 °C for 3 hours and cooling the rail in the accelerated air flow which yields a fine fully pearlitic microstructure.

Specimens containing WELs were carefully ground after cutting with a low speed diamond saw in order to avoid microstructural alterations due to specimen preparation. Afterwards, the specimens were carefully polished with solutions containing 3 μm and 1 μm diamond particles respectively, to remove the deformation layer from grinding. The specimens were then etched using 2% Nital solution to identify the WEL structure in the light optical microscope (Keyence VHX 6000). The WELs offer a higher resistance to chemical etching in comparison to the base pearlitic microstructure. Hence, chemical etching resulted in a better visibility of the WELs in the Scanning Electron Microscope (SEM) during the microcantilever preparation. The Vickers microhardness measurements were performed by a Dura-scan 70 (Struers) hardness tester using a load of 0.25 N for 10 s.

All microcantilevers in this study were prepared with their length parallel to the rail surface and at a depth of approximately 10 μm from the rail surface within the WELs. The microcantilever are produced by mechanical polishing of the rail surface and followed by FIB milling. Micro-cantilevers of approximately 4 x 4 x 28 μm^3 were cut via FIB milling using a FEI Helios Dual Beam FIB microscope with an acceleration voltage of 30 kV. The 2.5 nA ion current was used for coarse milling, while intermediate milling was performed with an 86 pA ion current. Please note that higher currents cause severe re-deposition on the cantilever surface, which generates artefacts during mechanical testing. Thus, a final cleaning was performed with 40 pA ion current to remove the re-deposited layer. Afterwards, Electron Backscatter Diffraction (EBSD) analysis was performed on the cantilevers using a JEOL JSM 6500F SEM (SEM) to capture the WEL microstructure. All EBSD measurements were performed at an accelerating voltage of 15 kV, working distance of 18 mm, and a step size of 40 nm. The EBSD data was analysed using Orientation Image Microscopy (OIM) software (TSL-OIM). Bridge notches were cut in the Zeiss Auriga® dual beam microscope equipped with a Nano Patterning and Visualization Engine (NPVE). A thin bridge was left on both

sides of the artificial notch created by FIB milling. The bridge-notch configuration leads to the highest stresses in the notch, which fail first and result in a sharp and uniform crack along the notch plane.

These notches were prepared with a 10pA current and a 20 nC/μm^2 dose. The notch depth is in the range of 700 – 800 nm in different cantilevers.

The *in situ* micromechanical tests were performed in a Zeiss Gemini 500 SEM microscope. The experiments were performed in a displacement controlled mode (0.02 μm/s) using a conductive diamond wedge indenter (ASMEC UNAT-II) with an opening angle of 60° and 10 μm wedge length. Videos of the crack propagation and cantilever deformation were recorded (see supplementary information).

The fracture toughness of the WELs was calculated by i) Matoy's *et. al.* LEFM approach [28] and ii) Wurster's *et.al.* EPFM approach [33].

LEFM was used to calculate the conditional stress intensity factor (K_{IQ})

$$K_{IQ} = \frac{F_Q\, L}{B\, W^{3/2}}\, f(a/W) \tag{1}$$

$$f\left(\frac{a}{W}\right) = 1.46 + 24.36\left(\frac{a}{W}\right) - 47.21\left(\frac{a}{W}\right)^2 + 75.18\left(\frac{a}{W}\right)^3 \tag{2}$$

where F_Q is the critical force, L is the bending length, a is the notch depth that is interpreted as the initial crack length, B is the cantilever thickness, W is the cantilever width and $f(a/W)$ is the shape factor for the specimen geometry [33].

The conditional linear elastic stress intensity factor K_{IQ} is determined here (as opposed to the linear elastic fracture toughness K_{IC}) because the constraints on the sample geometry according to the ASTM Standards are not fulfilled in these experiments. In addition, the EPFM approach by Wurster *et al.* [33] was used to calculate the conditional fracture toughness ($K_{IQ,J}$) for WELs. This approach is detailed in Sec.3.2.

After *in situ* micromechanical testing, cantilevers were polished using a 40 pA ion current and an approximate 1 μm layer was removed from the cantilever in a FEI Helios Dual Beam FIB. Afterwards, EBSD and SEM imaging of the fracture surface and crack morphology were carried out in a JEOL JSM 6500F SEM. The EBSD scans were used to characterize the microstructural changes in the WELs during crack growth.

Correlative Transmission Electron Microscopy (TEM) and Atom Probe Tomography (APT) measurements were conducted at a similar depth in the WEL (*i.e*. 10 μm below the rail surface) where micro fracture experiments were conducted. [35–40]. On the APT specimens, TEM analysis was carried out using a Philips CM-20 operated at 200 kV. After TEM inspection, the specimens were measured for near-atomic-scale compositional analysis in the APT. APT measurement were conducted using a LEAP 5000XS (CAMECA Instruments). The instrument was operated in laser pulsing mode at a rate of 200 kHz and with a pulse energy of 40 pJ. The specimen's base temperature was 50 K and the target detection rate was set to 5 ions per 1000 pulses. Data analysis was performed using the software package IVAS 3.6.12.

3. Results and discussion

3.1 Failure in rails due to the White Etching Layers (WELs)

Fig. 1(a) is an optical micrograph showing the brittle failure of the WEL followed by fatigue crack propagation into the deformed and undeformed pearlitic matrix. The crack in the matrix grows at an angle of around 38° to the loading direction (opposite to the X direction in Fig. 1(a)), which is close to the direction of maximum resolved shear stresses (*i.e.* 45°). However, the crack in the WEL seems unaffected by the maximum resolved shear stresses and grows by brittle cleavage (Fig. 1(a)). The WELs are harder than the base pearlitic matrix: Fig. 1(b) shows the variation of micro hardness from the rail raceway into the rail matrix material. The hardness in the WEL is maximum (1000 ± 25 HV) close to the rail raceway and decreases towards the base matrix (Fig. 1(b)). The hardness is 710 ± 20 HV close to WEL/deformed pearlite interface. The maximum thickness of the WEL in this case is around 80 μm.

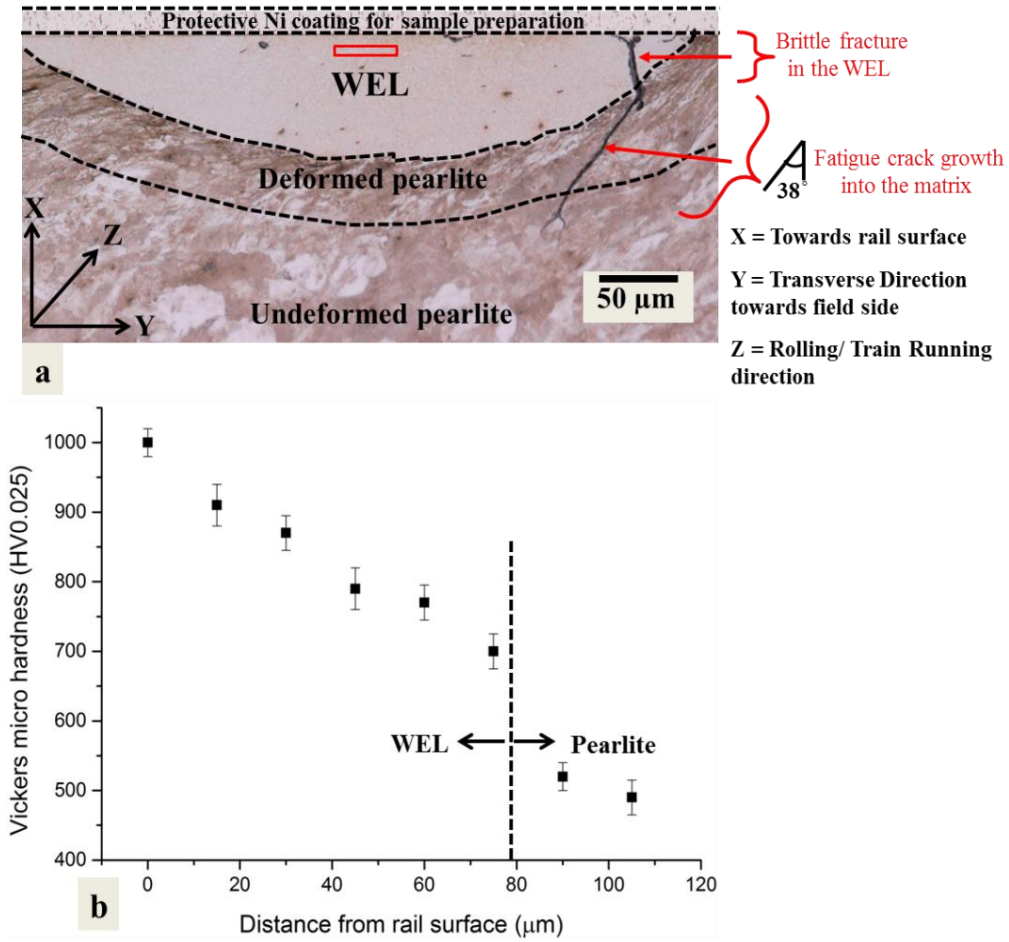

Fig. 1. Optical micrograph of brittle cleavage in the white etching layer that formed at the rail surface and crack propagation into the base pearlitic matrix. The red rectangle shows the position of the micro-cantilevers, (b) Micro hardness from the rail surface to the depth.

3.2 Calculation of fracture toughness of the WELs

The schematic of the microcantilevers and the coordinate system of the cantilever with respect to the rail are shown in Fig. 2(a). The intended crack plane in the microcantilevers is parallel to the XZ plane (Fig. 2(a)) where X is the rail surface normal and Z is the train running direction. A representative force (F) displacement (d) curve from the WEL microcantilever is shown in Fig. 2(b), in which the repeated loading/unloading sequences are used to measure the cantilever compliance and deduce the crack propagation evolution. The crack propagation at various steps (at 6 µm, 8 µm, 12 µm, and 15 µm) during the *in situ* microcantilever deformation are shown in Fig. 2(c-h). The force-displacement curve and crack tip behaviour highlight the elastic-plastic response of the WEL. The observed plasticity is attributed to the large plastic zone size and the complex microstructure of the WELs (discussed later in Sec. 3.6). The crack branching and micro-dimples are also observed (Fig. 2(h)), which reduce the effective crack intensity ahead of the primary crack tip and decrease the local driving force for crack propagation [41,42]. The complete fracture process of the WELs can be seen in the

experimental videos attached in supplementary information. When applying LEFM (according to Eq. 1 and 2) to the force-displacement curve shown in Fig. 2(b), the linear elastic fracture toughness (K_{IQ}) of the WEL is determined as 4.2 ± 0.6 MPa√m (error margin is estimated from statistical error propagation).

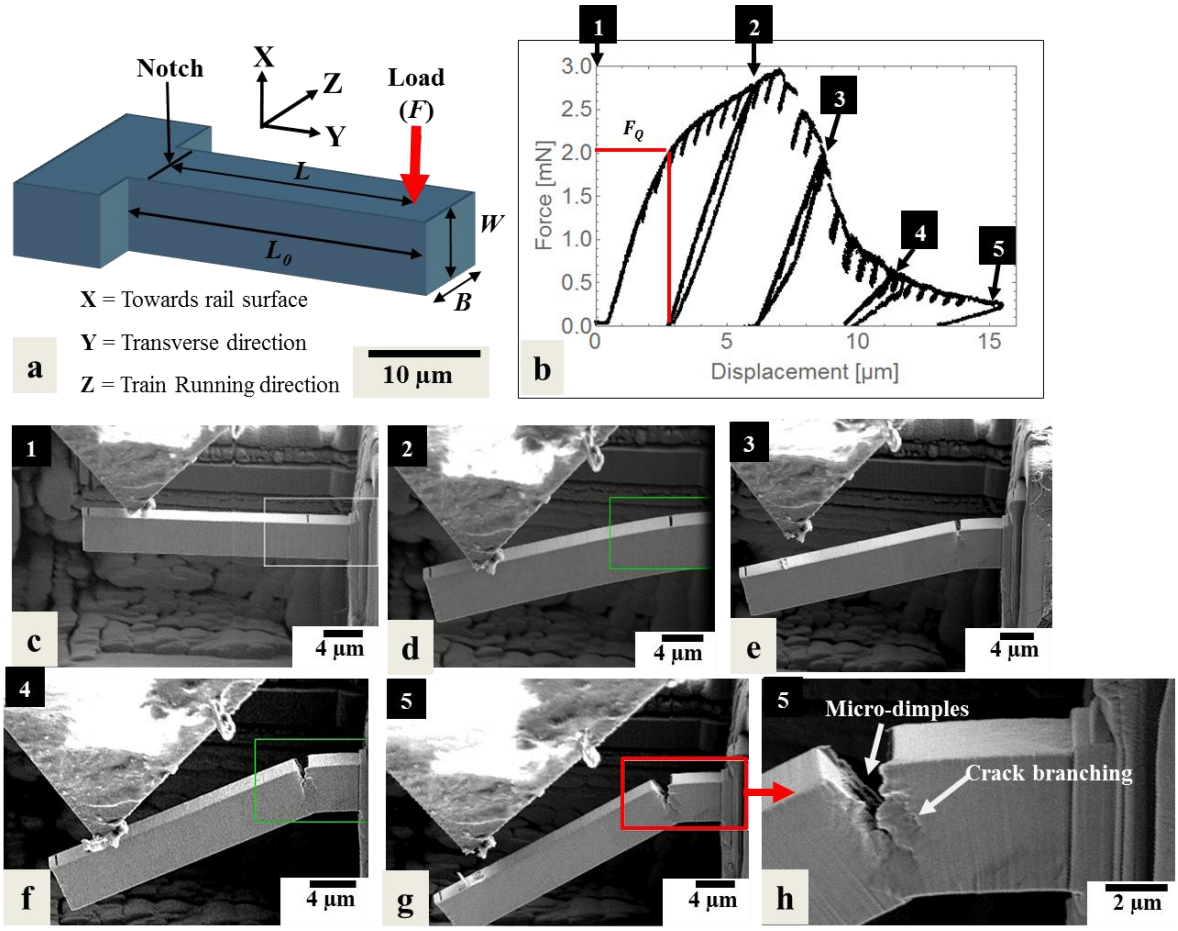

Fig. 2. ***In situ micro-cantilever deflection experiments.*** (a) schematic of the microcantilever used for *in situ* bending, (b) Load-displacement (*F-d*) curve of the WEL marked with four intermediate deformation steps (6 µm, 8 µm, 12 µm, and 15 µm), (c) WEL microcantilever before start of bending test, (d-g) SEM images of cantilever during four intermediate deformation steps *i.e.* (d) 6 µm, (e) 8 µm, (f) 12 µm and (g) 15 µm, (h) magnified SEM image of the WEL cantilever after 15 µm displacement, showing crack branching and micro-dimples on the fracture surface.

Significant plasticity is observed in the cantilever, as shown in Fig. 2(b). Thus, an elastic-plastic approach by Wurster *et al.* [33], is used to quantify the fracture toughness of the WEL. The unloading stiffness of cantilever is determined for each unloading segment and plotted against the displacement, as shown in Fig. 3(a). The cantilever stiffness continuously decreases with indenter displacement (Fig. 3(a)). The cantilever stiffness at each unloading step determines the instantaneous crack length (a_i), as evaluated by equation 3

$$a_i = W - \sqrt[3]{\frac{4\,k_i\,L^3}{B\,E}} \quad (3)$$

where a_i is the crack length at the i^{th} unloading step of unloading, W is the cantilever width, k_i is the cantilever stiffness at the i^{th} unloading step, B is the cantilever thickness, E is the elastic modulus.

Fig. 3(b) shows the crack length plotted against the cantilever displacement (data points in red). This data shows that the crack length increases monotonically with the displacement. Afterwards, the J integral is calculated as a sum of elastic and plastic components:

$$J_{(i)} = \frac{(K_{IQ(i)})^2(1-\nu^2)}{E} + \frac{\eta\,A_{Pl(i)}}{B\,(W-a_0)} \quad (4)$$

where $K_{IQ(i)}$ is the conditional stress intensity factor at the i^{th} instant calculated from Eqs. (1) and (2), η is a constant equal to 2, and ν is the Poisson ratio taken as 0.3. $A_{Pl(i)}$ denotes the area under the load-displacement curve Fig. 2(b).

The crack resistance curve is shown in Fig. 3(c), *i.e.* the crack extension against J integral. The initial linear segment of the curve is known as blunting line (initial slope), where the artificial FIB milled notch starts to become a natural crack and the later segment represents stable crack growth, where the crack transitions from crack blunting to a real crack surface and stable crack growth becomes dominant. The J integral at intersection point of both lines is the critical J integral (J_c) (Fig. 3(c)) according to Wurster *et al.* [33], which is used to calculate the fracture toughness ($K_{IQ,J}$)[1]:

$$K_{IQ,J} = \sqrt{\frac{J_c\,E}{1-\nu^2}} \quad (5)$$

[1] The translation from J_c to $K_{IQ,J}$ is based on the plane strain assumption.

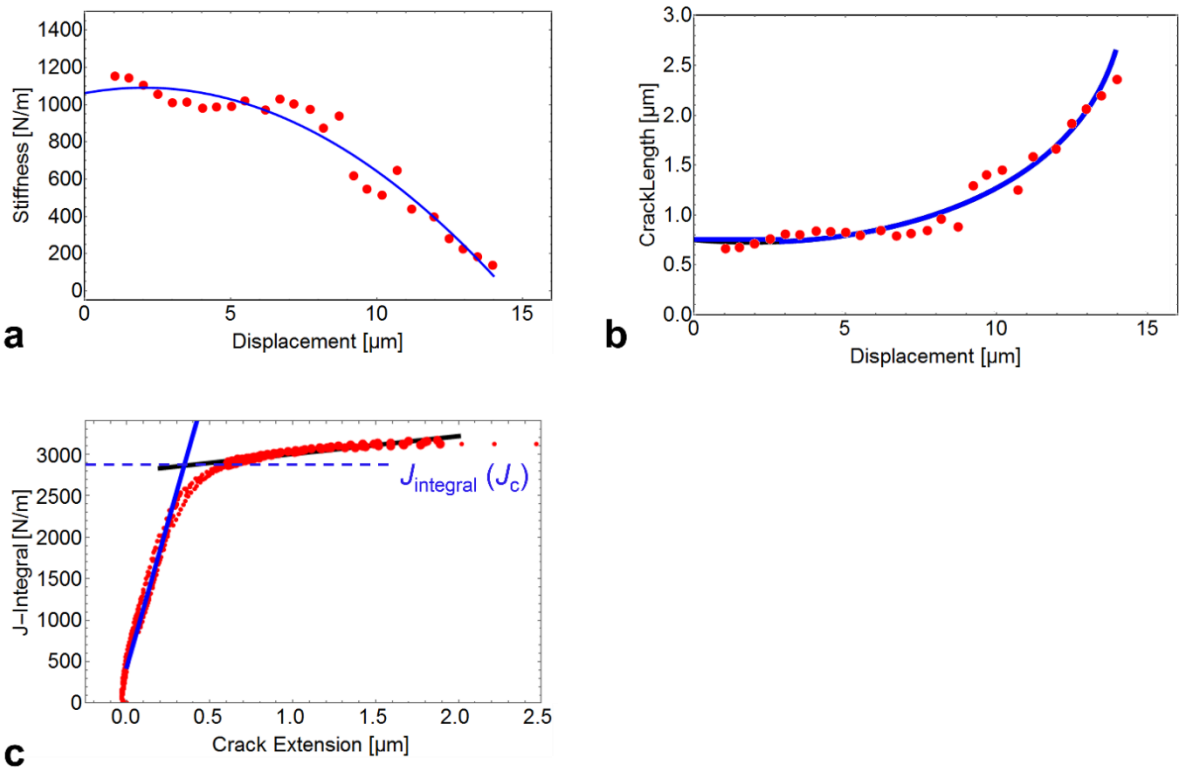

Fig. 3. ***Elastic-plastic fracture mechanics approach.*** (a) Stiffness variation of the micro-cantilever with respect to displacement, (b) Crack growth/extension with respect to cantilever displacement derived from unloading compliances of the micro-cantilever, (c) Variation of *J*-integral vs crack extension.

The critical J-integral is approximately 2900 N/m which corresponds to a conditional fracture toughness ($K_{IQ,J}$) of 25.4 ± 2.3 MPa√m for the WEL **(**error margin is estimated from statistical error propagation). It should be noted that the obtained conditional toughness depends on the geometry and definition of J_c. A thorough discussion about this can be found in [43].

The fracture toughness values from four WEL microcantilevers show significant plasticity, as shown in Table 1. It is observed that the linear elastic fracture toughness K_{IQ} for WELs is in the range of 4.2 – 7.6 MPa√m, whereas the $K_{IQ,J}$ vary from 21 – 25 MPa√m.

Table 1. Fracture toughness according to LEFM and EPFM (K_{IQ} and $K_{IQ,J}$) of the WEL cantilevers, with corresponding dimensions, notch size, and calculated J integral values. Cantilever 4 is shown in Fig. 2. (Error margins are estimated from statistical error propagation).

Sample Number	Dimensions (B x W x L) μm^3	Notch size a (μm)	Linear elastic fracture toughness K_{IQ} (MPa√m)	J-integral (N/m)	Fracture toughness (EPFM) $K_{IQ,J}$ (MPa√m)
Cantilever 1	3.7x4.2x20	0.74	5.9 ± 0.9	2075	21.5 ± 3.5
Cantilever 2	3.6x3.9x22	0.69	7.6 ± 1.1	2420	23.2 ± 3.3
Cantilever 3	4.2x4.3x23	0.79	6.0 ± 0.9	2600	24.0 ± 3.4
Cantilever 4	4.1x4.1x19	0.75	4.2 ± 0.6	2890	25.4 ± 2.3

Based on the fracture toughness values given in Table 1, the WELs show an average K_{IQ} of 5.9 ± 0.6 MPa√m and an average $K_{IQ,J}$ of 23.5 ± 0.7 MPa√m. The error margins are expressed as standard error of the mean.

3.3 Fracture surface analysis and crack blunting in the WELs

Fig. 4 shows the fracture surface images of the cracked cantilevers 1 and 2 from Table 1. Fig. 4(a) highlights crack blunting, which is an indication of plasticity induced crack arrest. Microdimples are also observed on the fracture surfaces of all cantilevers (Fig. 4(a,b)).

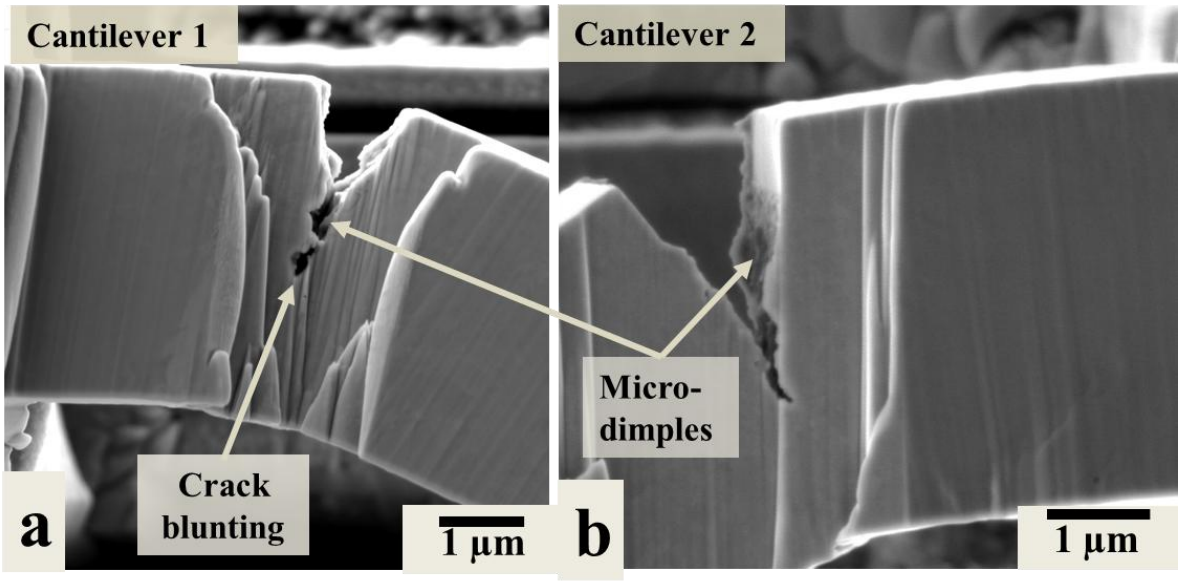

Fig. 4. (a-b) Fracture surface images of the cracked cantilevers 1 and 2 showing crack blunting and the presence of microdimples.

3.4 Comparison of fracture toughness of WELs with other Fe-based alloys

Table 2 shows the comparison of fracture toughness of the present WEL specimens and of Fe-based alloys from literature [29,42,44,45]. It is worth to mention that the comparison is difficult due to the large differences in the chemical composition, processing routes and the microstructural features (*i.e.* grain sizes, phase constituents, *etc.*). Additionally, the limited data on the fracture toughness at the microscale, the lack of standardization at small dimensions dissatisfying ASTM standards and differences in the specimen sizes further complicates the precise comparison. However, the comparison shows the range of variation in Fe-based alloys.

The WELs formed from an initially fully pearlitic microstructure in the rails. We compare the reported fracture toughness of the WELs to that of undeformed pearlitic steels. Hohenwarter *et al.* [44] showed that fully pearlitic steels at the macroscale, with interlamellar spacing of around 200 nm, display ductile failure with a fracture toughness K_{IC} = 53 MPa√m (Table 2). This value is larger than the conditional fracture toughness ($K_{IQ,J}$) of the WELs (21 – 25 MPa√m) reported in this study. This comparison indicates that the WELs are brittle in comparison to undeformed pearlitic steels.

Most of the previous studies suggest that the WELs are primarily consisting of martensite in their microstructure [3,7,46]. Thus, we compared the fracture toughness of the WELs to that of a martensitic microstructure. Saxena *et al.* [43] carried out micro fracture investigations on the quenched martensite having the same chemical composition as pearlitic rail steels, which are studied in the present work. The measured $K_{IQ,J}$ values of quenched martensite were 16-18 MPa√m [43] (following the fracture toughness approach of Wurster *et al.* [33] and Pippan *et al.* [47]). WELs show slightly higher values (21-25 MPa√m) than the quenched martensite. The difference in fracture toughness of the WELs and the quenched martensite is attributed to the differences in their microstructural features such as grain size, C saturation in the martensitic matrix and dislocation densities *etc*[2]. Additionally, in comparison to the quenched martensite, WELs undergo many microstructural changes overtime during different wheel-rail contacts [19]; where each wheel-rail contact applies a different loading condition due to the difference in local contact parameters such as wheel/rail roughness, friction coefficient, train velocity, axle load *etc*. However, the quenched martensite studied in [43] has undergone a single heat treatment cycle with heating just above the austenitization temperature and rapid

[2] The microstructure of the WELs is discussed later in Sec. 3.6 and the microstructural information of quenched martensite is given in the supplementary material.

cooling to the room temperature. The difference in the aforementioned local loading conditions in rails can lead to differences in the WEL microstructures which is one of the reasons for the scatter in WEL fracture toughness values (Table 1).

The fracture toughness of WELs is further compared to the toughness of nanocrystalline heavily drawn pearlitic steels wires (Table 2), due to some similarities between their microstructures. The WELs on the rail surface are formed due to the combined effect of temperature rise above the austenitization temperature followed by fast cooling, and heavy plastic deformation [17–19]. The microstructure of the WELs primarily consists of the martensite phase (having body centred tetragonal crystal structure) with some austenite and partially dissolved parent cementite. Therefore, the presence of martensite and plastic deformation under wheel-rail contact both contribute to a high dislocation density in the WEL microstructure [6,17–19]. Similarly, the heavily drawn pearlitic wires show a high dislocation density, the presence of partially dissolved cementite and strain-induced increase in tetragonality in the ferritic matrix [48]. Due to these similarities, the heavily drawn pearlitic wires are a good system for comparison with the WELs. Jaya *et al.* [45] showed that heavily drawn pearlitic wires at ε = 3.2 show elastic-plastic rupture with a conditional fracture toughness $K_{IQ,J}$ = 27 MPa√m (Table 2) in the wire drawing direction. That value is close to the fracture toughness of the WELs measured in the current study ($K_{IQ,J}$ = 21 – 25 MPa√m). The fracture toughness of the heavily drawn wires decreases with the increase in drawing strain. The wires show linear elastic fracture and brittle fracture surfaces for drawing strains of 4.2 (K_{IQ} = 5.2 MPa√m) and 5.2 (K_{IQ} = 4 MPa√m) (Table 2). Hohenwarter *et al.* [29] showed that fracture toughness of these wires depends strongly on the crack growth direction with respect to the wire axis. The fracture toughness ($K_{IQ,J}$) of these wires is around 40 MPa√m at ε = 3.1 and 21 MPa√m at ε = 6.5 in the direction perpendicular to the wire axis (Table 2). The WELs are not expected to show similar anisotropy in the fracture toughness because of the absence of texture and the equiaxed grain shape [19].

We compare the WEL fracture toughness to that of ductile ferrite (BCC iron) and brittle nanocrystalline Fe thin films. Hohenwarter *et al.* [42] measured the fracture toughness (K_{IC}) of 202 MPa√m for Fe with an average grain size of 38 μm (Table 2). Nanocrystalline sputtered Fe thin films shows highly brittle rupture: K_{IQ} = 2 MPa√m [45] (Table 2).

Based on those comparisons and based on the experimental evidence of plasticity in the microcantilever tests, it is concluded that the WELs are neither as ductile as Fe or pearlitic

steels nor as brittle as nanocrystalline Fe thin films or heavily drawn pearlitic wires when tested in the drawing direction. The WELs rather show semi-brittle fracture response with intermediate fracture toughness values ($K_{IQ,J}$ = 21 – 25 MPa√m) which lie close to fracture toughness of the quenched martensite.

Table 2. Comparison of fracture toughness values of the WELs with other Fe based alloys [29,42–45]. The lower boundary of the fracture toughness (K_{IQ}) is calculated from linear elastic assumptions. The conditional fracture toughness ($K_{IQ,J}$) is the lower bound plus the correction according to the plastic hinge model of Wurster *et al.* [33]. The fracture toughness K_{IC} fulfils all criteria of the ASTM standards.

Materials	Linear elastic fracture toughness K_{IQ} (MPa√m)	Fracture toughness $K_{IQ,J}$ (MPa√m)	Fracture toughness K_{IC} (MPa√m)	Testing method
WELs (grain size $d \approx 350 \pm 260$ nm)	4.2 – 7.6	21 – 25	-	Micro cantilever tests
Pearlitic steels [44] (200 nm interlamellar spacing)	-	-	53	Macro scale tests
Quenched Martensite [43] ($d \approx 300 \pm 250$ nm, see supplementary information)	-	≈ 16 – 18	-	Micro cantilever tests
Nanocrystalline pearlitic steels at different true strain (ε) [45] (in the drawing direction)	7.5 (ε = 3.2, $d \approx$ 18 nm)	27 (ε = 3.2, $d \approx$ 18 nm)	-	Micro cantilever tests
	5.2 (ε = 4.2, $d \approx$ 15 nm)	-	-	Micro cantilever tests
	4 (ε = 5.2, $d \approx$ 10 nm)	-	-	Micro cantilever tests
Nanocrystalline heavily drawn pearlitic steels at different true strain (ε) values (perpendicular to drawing direction) [29]	-	40 (ε = 3.1, $d \approx$ 20 nm)	-	Single edge notched tension tests, CTOD
	-	21 (ε = 6.5, $d \approx$ 10 nm)	-	Single edge notched tension tests, CTOD

Nanocrystalline heavily drawn pearlitic steels at different true strain (ε) values (in the drawing direction) [29]	5.0 (ε = 3.1, $d \approx$ 20 nm)	-	-	Micro cantilever tests
	3.7 (ε = 6.5, $d \approx$ 10 nm	-	-	Micro cantilever tests
Pure BCC Fe ($d \approx$ 38 μm) [42]	-	-	202	Macro scale tests
Nanocrystalline sputtered Fe thin films ($d \approx$ 200 nm) [45]	2	-	-	Micro cantilever tests

3.5 Consequence of fracture toughness of WELs

The obtained fracture toughness values of the WELs can be used to estimate the critical defect size ($a_{critical}$), which is required for crack propagation at an assumed stress state [43]. The value of $a_{critical}$ is estimated using

$$K_Q = Y\sqrt{\pi a_{critical}}\,\sigma_y \quad (6)$$

where Y is a dimensionless geometry factor taken to be 1[43], σ_y is the yield strength. Using the macroscopic yield strength (σ_y = 811 MPa from [49]) and fracture toughness (53 MPa√m from Table 2) of pearlitic steels, the value of $a_{critical}$ is approximately 1360 μm.

As the WELs are primarily consisting of martensite in their microstructures [19] and the fracture toughness of WEL is close to that of quenched martensite, the yield strength of martensite is utilized to determine the $a_{critical}$ value for the WELs. The value of σ_y for martensite is approximately 1800 MPa for 0.72 wt.% C [50] which is also the C concentration in pearlitic rail steels studied in the present work. Using σ_y = 1800 MPa and the fracture toughness values of WEL as 21-25 MPa√m, the $a_{critical}$ for the WELs is approximately in the range 40-60 μm. As shown in Table 2, the fracture toughness of WELs is approximately 53-60% less than that of undeformed pearlitic steels. In addition, the estimated critical defect size in the WELs is significantly smaller than the undeformed pearlitic steels. Based on this analysis, the formation of WELs in pearlitic rail steels is detrimental for the rails.

3.6 Microstructural features affecting the fracture behaviour of the WELs

Crack growth is a complex process in polycrystalline materials as it involves dislocation motion, dislocation pile ups at obstacles, crack tip blunting, work hardening, atomistic bond breaking *etc.* [51]. Various microstructural features such as grain size, grain orientations, phase fractions, grain/phase boundaries, dislocation density *etc.* affect the crack initiation and growth. The WELs consist of an intricate microstructure due to complex rail-wheel contact [19]. Fig. 5 shows the EBSD Inverse Pole Figure (IPF), phase and Kernel Average Misorientation (KAM) maps of microcantilever 4 before (Fig. 5(a)) and after (Fig. 5(b)) the *in situ* fracture tests. KAM maps were generated by taking the 2nd nearest neighbouring pixels with a maximum misorientation of 5°. It should be noted that the EBSD on the fractured cantilever is performed after removing a 1 μm thick slice from its surface as it is not possible to obtain the Kikuchi patterns directly on a deformed cantilever. Hence, the measured area after fracture is not the same as before fracture. We observe mixed intragranular and intergranular crack growth in the WEL in Fig. 5(b). The phase map in Fig. 5(a) shows the presence of austenite (in green) within the WEL cantilever. The austenite area fraction is initially approximately 3-4% before the *in situ* experiments. The EBSD measurements did not show austenite in the vicinity of the crack after the *in situ* test (phase map in Fig. 5(b)). This observation is evidence for strain-induced austenite to martensite transformation during the crack growth.

The KAM map of the WEL in Fig. 5(a) shows martensitic areas with low KAM (0.39-0.49°) (indicated by black arrows). These areas can be envisaged to have undergone dynamic recovery in martensitic microstructure of the WELs due to temperature rise under the wheel-rail contacts [19]. Such low KAM areas are not observed after the fracture experiments on the WEL. The KAM map in Fig. 5(b) shows no sign of a distinguishable plastic zone in the vicinity of the crack after fracture in the WEL cantilever. The KAM maps in Fig. 5 show that the average KAM increases from 0.82 ± 0.54° to 0.85 ± 0.56° before and after fracture (± 0.54° and ± 0.56° are the standard deviation values). These KAM values are used to calculate the Geometrically Necessary Dislocation (GND) density using

$$\rho_{gnd} = \frac{\alpha\theta}{ub} \tag{7}$$

where α is a constant (α = 3 for mixed dislocations [52]), θ is the average KAM angle, u is the distance between misoriented points, which is the step size in EBSD map (*i.e.* 4 x 10^{-8} m), b is the magnitude of the Burgers vector (*i.e.* 2.47 x 10^{-10} m).

The GND density in cantilever 4 changes from $4.3x10^{15}$ to $4.5x10^{15}$ m^{-2} after the *in situ* fracture test which is not a pronounced change. This is attributed to the presence of a high density of defects and interfaces in the WEL [19] (Fig. 5). This observation also leads to a conclusion that the plastic zone in the vicinity of crack in WEL is small and concentrated near the notch (discussed later in Fig. 6). Thus, a significant change in the average GND values is not observed.

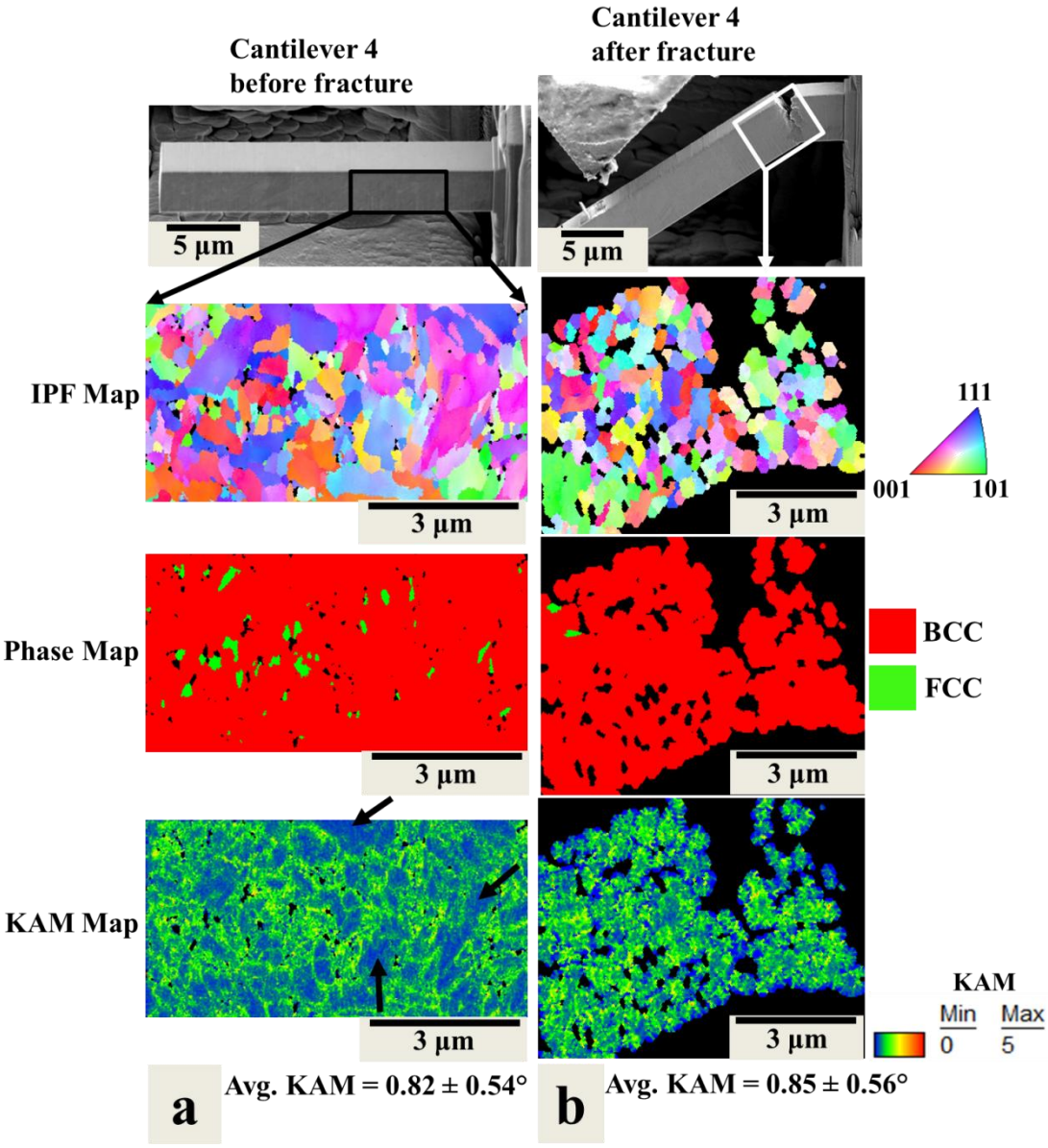

Fig. 5. EBSD results showing IPF, phase and KAM maps from the cantilever 4: (a) before (b) after the *in situ* experiments. (Black colour arrows in the KAM map of WEL cantilever before fracture, show the martensitic grains with low KAM value (0.38-0.49°))

Additional EBSD investigations were performed on cantilever 1 before and after fracture (Fig. 6). Alike cantilever 4, the observations show mixed intergranular and intra-granular fracture and strain-induced austenite to martensite transformation during the crack growth in cantilever 1 (as displayed in the IPF and phase map in Fig. 6(b)). We observe that the average KAM in cantilever 1 is 0.88°, with a standard deviation of ± 0.57°, before fracture (Fig. 6(a)), which corresponds to a GND density of 4.66 x 10^{15} m^{-2}. The KAM map in Fig. 6(a) displays low KAM areas (0.39-0.50°) (indicated by black arrows), which are not visible after the fracture experiments (Fig. 6(b)) as previously observed in cantilever 4 (Fig. 5).

Unlike cantilever 4, the KAM map from cantilever 1 (Fig. 6(b)) shows an area (enclosed in red lines) with a high average KAM of 0.96 ± 0.51° in the crack vicinity. This misorientation corresponds to an increased average GND density of 5.10 x 10^{15} m^{-2} (Eq. 7). This high GND density area can be attributed to the plastic zone near the crack. The observed plastic zone shape is complex due to the complex WEL microstructure containing grains with different sizes and orientations. The average KAM outside the plastic zone is 0.91°, with a standard deviation of ± 0.52°, which corresponds to a GND density of 4.82 x 10^{15} m^{-2}.

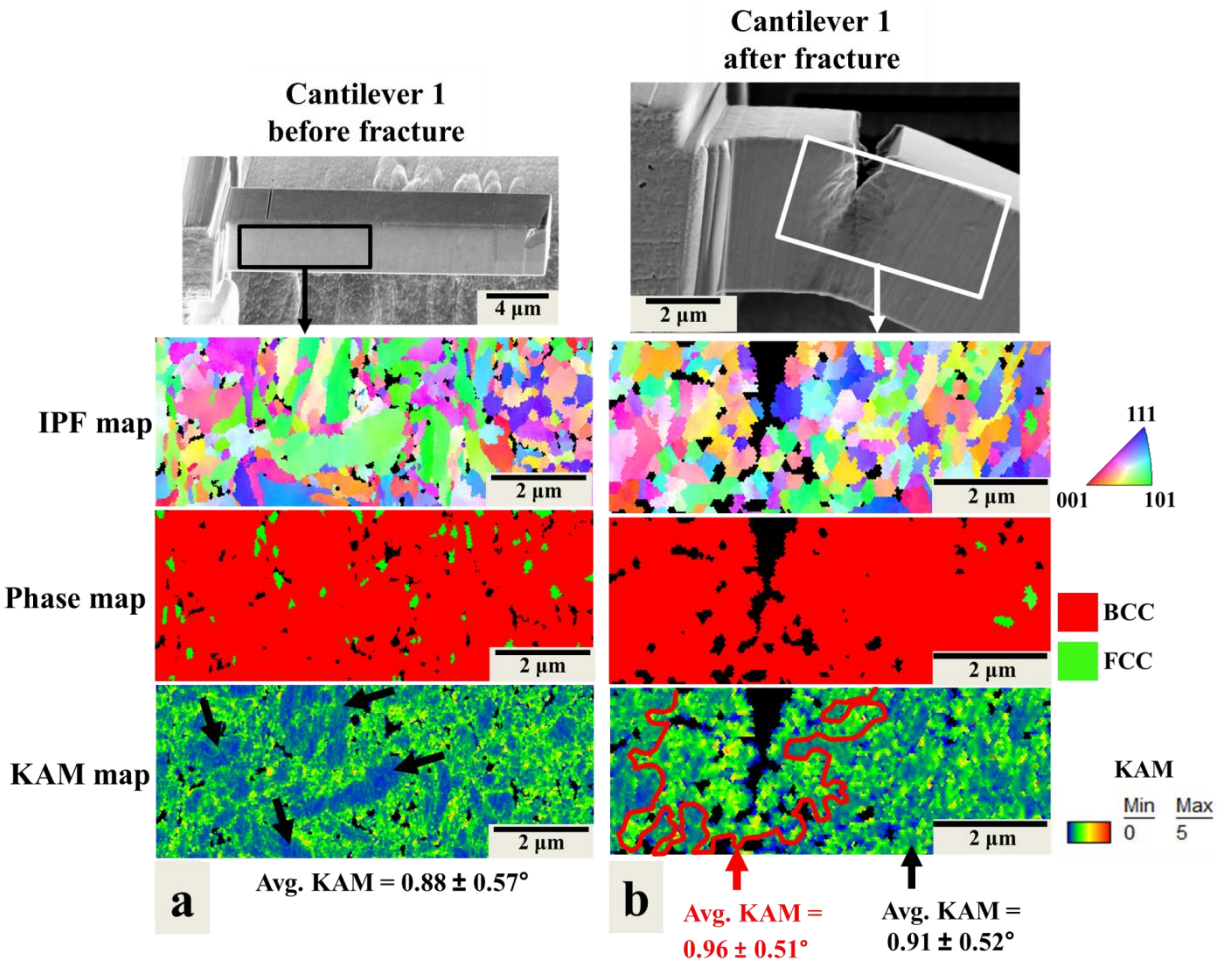

Fig. 6. EBSD results showing IPF, phase and KAM maps from the cantilever 1: (a) before and (b) after fracture. (Black colour arrows in the KAM map before the test show the martensitic grains with low KAM (0.39-0.50°)) (The high KAM area (enclosed in the red lines) on the KAM map in Fig. 6(b) represents the plastic zone associated with the crack).

The microstructural features, responsible for semi-brittle nature of the WELs and observed plastically in the WELs in *in-situ* tests, are further discussed below.

3.6.1 Presence of austenite and its transformation into martensite during crack growth

The presence of austenite phase in the microstructure of WELs (EBSD phase map in Fig. 5(a) and Fig. 6(a)) is one of the reasons for the observed plasticity in the *in situ* fracture toughness experiments. This is because of the easy tendency of slip of the austenite phase due to its Face Centred Cubic (FCC) crystal structure in comparison with martensite with Body Centred Tetragonal (BCT) structure. We observe a reduction in austenite phase fraction before and after *in situ* fracture experiments (EBSD phase maps in Fig. 5 and Fig. 6). This reduction in austenite fraction is attributed to strain-induced transformation of austenite into martensite during the crack growth in the WELs. This transformation can result in crack closure during the crack growth in the WEL due to the crystal volume expansion concerning austenite (FCC) to martensite (BCC) transformation. In addition, this transformation relaxes the stress intensity ahead of the crack tip and causes the retardation in crack growth and hence contribute to increase the fracture toughness [53,54]. Hornbogen *et al.* [55] studied the effect of austenite to martensite transformation ahead of a fatigue crack on the Fatigue Crack Growth Rate (FCGR). They proposed retardation in FCGR ($\frac{da}{dN}$) due to austenite to martensite transformation using

$$\frac{da}{dN} = B\frac{(\Delta K)^4}{(\sigma_y)^2\, E\, (U_p+U_t)} \tag{8}$$

where, B is a dimensionless constant, ΔK is the applied stress intensity range, σ_y is the yield strength, E is elastic modulus, U_p is the energy required for fatigue crack propagation and U_t is the energy required for strain-induced austenite to martensite transformation. Hence, the crack growth in the WEL will be retarded due to austenite to martensite transformation as this transformation requires an excess energy U_t in the denominator of Eq. 8. Hornbogen *et al.* [55] also estimated the retardation in fatigue crack growth due to the volume expansion

caused by austenite to martensitic transformation in the vicinity of the crack. The resulting compressive stresses (σ_t) (due to this transformation) induced ahead of the crack tip is given by

$$\sigma_t = -E\frac{\Delta v}{3v}f_t \quad (9)$$

where E is the elastic modulus (200 GPa), $\Delta v/v$ is the volume expansion caused by the transformation, and f_t is the fraction of austenite transformed into martensite.

The WEL contains 3-4% austenite (Fig. 5) in its microstructure. If an austenite island is in front of a sharp crack tip and assuming that the size of the austenite is large in comparison to the size of the crack tip, f_t can be assumed to be 1. During austenite to martensite transformation, the magnitude of $\Delta v/v$ is approximately 0.04 for the 0.72 wt.% C steel (same C content in pearlitic steels studied in this work) [56]. This volume expansion will result in a compressive stress of approximately 2600 MPa at the crack tip. The compressive stress will reduce the crack driving force and will lead to crack retardation. It should be noted that the calculated stress is the upper boundary for the compressive stress due to austenite to martensite transformation in the WELs. The exact value of this stress would be challenging to estimate due to the large number of unknown variables such as austenite size, spatial distribution of austenite around the crack tip and their crystallographic orientation *etc.* Additionally, the probability of the austenite to fall in the vicinity of the crack should also be considered.

3.6.2 Grain size, dislocation density and dislocation annihilation in martensitic grains

The fracture toughness is strongly affected by the grain size and the dislocation density in the material microstructure [42,44,45,57]. Jaya *et al.* [45] studied the influence of the grain size and dislocation density on the fracture toughness of cold drawn pearlitic steels. They showed that the fracture toughness (K_{IQ}) decreases from 7.5 to 4 MPa√m with the increase in drawing strain from 3.2 to 5.2. This is attributed to a decrease in average grain size from 18 to 10 nm, increase in dislocation density and increased carbon (C) supersaturation in the matrix (Table 2) [45]. Additionally, the fracture becomes more brittle with increase in drawing strain. It should be noted that it is difficult to delineate the effect of grain size, dislocation density and C supersaturation on the fracture response. We discuss the effect of grain size and dislocation density in this section whereas the C super saturation is discussed later in Sec. 3.6.3.

Zhang *et al.* [58] showed a dislocation density of around 1.4 x 10^{16} and 4.5 x 10^{16} in cold drawn pearlitic wire at the drawing strain of 3.2 and 5.2, respectively. Similar order of dislocation density was quantified in the WEL using synchrotron X-ray diffraction in [9]. Additionally, we investigated the microstructure of the quenched martensite (see supplementary information). The quenched martensite shows the average KAM values of 0.87 ± 0.56° which are of the same order of magnitude as the WELs (Fig. 5 and Fig. 6). This finding implies that the WELs and quenched martensite have dislocation densities in the same order of magnitude. Hence, the contribution of dislocation plasticity to fracture can be considered similar for WELs, quenched martensite and cold drawn pearlitic wire. Therefore, we further discuss only the effect of grain size and C saturation in the matrix on the fracture response.

In case of WELs, we observe a large variation in grain sizes (as shown in the IPF maps in Fig. 5 and Fig. 6). The average grain diameter in the WEL is 350 ± 260 nm (260 nm is the standard deviation). Similarly, the quenched martensite shows a large variation in the average grain diameter 300 ± 250 nm (see supplementary information) which is of the same order of magnitude as in WELs. Therefore, the small difference in the fracture toughness values of quenched martensite and WELs (Table 2) is primarily due to the difference in C super saturation in their matrix which is further discussed in detail in Sec. 3.6.3. The grain size of the WELs is higher than that for the drawn pearlitic wires (10-20 nm). The presence of larger grains in the WELs is one of the reasons for their elastic-plastic semi-brittle response, in comparison to the drawn wires (Table 2).

Li *et al.* [59] showed an increase in ductility for cold drawn pearlitic wires after low temperature tempering. They attributed this observation to the dislocation density reduction by dislocation annihilation and rearrangement. Similarly, the WELs also undergo dynamic recovery in the martensitic grains by dislocation annihilation due to temperature rises under wheel-rail contact [19]. Such martensitic grains with low KAM values (0.39-0.50°) are observed in the KAM maps in Fig. 5(a) and Fig. 6(a) (shown by arrows). The GND density in these low KAM areas ranges from 2.07 x 10^{15} m^{-2} to 2.65 x 10^{15} m^{-2} (Eq. 7). The dislocations in these areas will be more mobile during the crack growth due to the lower GND density than the high GND density areas in the WELs. Thus, these low KAM areas will contribute to the plasticity in the martensitic matrix of the WEL and are one of the reasons for elastic-plastic semi-brittle fracture response of the WELs.

3.6.3 Segregation of carbon at grain boundaries and dislocations in the WELs

Fig. 7 shows the correlative Transmission Electron Microscopy (TEM) and Atom Probe Tomography (APT) measurements on the WEL from the same rail depth where fracture experiments are performed (10 μm below the rail surface). Fig. 7(a) shows the bright field TEM image of an APT tip from the WEL with a selected area diffraction pattern from the encircled area. A grain boundary is observed in the TEM image. The selected area diffraction pattern in Fig. 7(a) shows the single phase present in the APT tip, which indicates that the cementite phase from initial pearlitic microstructure is completely dissolved in the martensitic matrix here. The result also indicates that there is no secondary carbides precipitation in the WEL. The APT measurement of this tip shows carbon (C) grain boundary segregation in Fig. 7(b). The C concentration at the grain boundary reaches around 11.6 ± 1.0 at.%, as shown by the one dimensional concentration profile drawn perpendicular to the grain boundary plane (Fig. 7(c)). It should be noted that the region of interest for 1D concentration profile is taken in the maximum C concentration region at the grain boundary plane and relatively lower C concentrations also exist at the grain boundary plane. The martensitic matrix of the WEL shows a C concentration of around 3 at. %. A constant concentration of Mn (1.2 at.%) and Si (1.1 at.%) is found within the matrix and at the grain boundary (Fig. 7(c)). Another APT measurement from the same rail depth is also presented in the supplementary material which shows the similar observations like Fig. 7.

The C concentration in the WEL matrix is compared with the APT measurements from heavily drawn pearlitic wires [59–61]. Li *et al.* [60] reported that the ferritic matrix in the heavily drawn wires reaches a C concentration of 2 at.% at $\varepsilon = 5$ because of the presence of partially dissolved cementite within the matrix. In the rails, the cementite from original pearlitic microstructure is completely dissolved in the WELs at a depth of 10 μm (Fig. 7(a,c)). Thus, the martensitic matrix of WELs contain around 1 at.% higher C concentration than the ferritic matrix of heavily cold drawn pearlitic wires having deformation-induced tetragonality. This is one of the reason that the maximum hardness in the WELs (910 ± 25 HV at 10 μm below rail surface in Fig. 1(b)) is higher than the hardness in the drawn wires (550 ± 20 HV at $\varepsilon = 5$ [44]). It should be noted that the C atoms in the martensitic matrix of the WELs are not entirely in the interstitial sites but also segregate at vacancies and dislocations, which we discuss below.

As discussed in Sec. 3.6.2, the fracture toughness of WELs and quenched martensite is compared based on the C supersaturation in their microstructures. In the quenched martensite,

C remains in the matrix due to fast diffusionless martensitic transformation. The C concentration in quenched martensite should be same as the bulk C concentration of pearlitic steels (*i.e.* 3.25 at.% C) whereas WELs show a C concentration of 3 at.% in the matrix ((Fig. 7(c)). Kumar *et al.* [19] showed that the WELs undergo many microstructural changes during their life time due to different wheel-rail contacts as discussed in Sec 3.4. For example, the C atoms in the WELs redistribute to the crystal defects (grain boundaries and dislocations) from their martensitic matrix (Fig. 7(c)). This redistribution is attributed to the slight temperature rise at the rail surface during the wheel-rail contact [19]. It is well known that the C segregation at grain boundaries (as observed in the WEL in Fig. 7(b)) increases the grain boundary cohesion [36,61–63] and affects the fracture phenomenon in the Fe-based alloys [45]. Wu *et al.* [64] showed that the C segregation to the Fe grain boundaries reduces the free energy by 62 kJ/mol and thereby acts as strong cohesion enhancer. Hence, in the WELs, the observed grain boundary segregation of C (Fig. 7(b,c)) strengthens the grain boundaries and minimizes the intergranular fracture. Consequently, due to redistribution of C to the grain boundaries/dislocations, the C concentration in the martensitic matrix of the WELs decreases to around 3 at. %. This C decrease in the WEL matrix will increase the plasticity of the WELs with respect to supersaturated quenched martensite having 3.25 at. % C.

The C atom probe map overlapped with the 7 at.% C iso-concentration surfaces (in green) in Fig. 7(c) shows the regions with high C concentrations. These regions are attributed to the C segregation at dislocations (shown by arrows). Dislocations have a high interaction energy of around 0.8 eV/atom with the C atoms [65,66]. Hence, C atoms redistribute to the dislocations in the martensitic matrix of the WELs due to temperature rise at the rail surface [19]. The crack growth in metals involves dislocation motion (*i.e.* slip) ahead of the crack tip. Thus, any obstacle in dislocation motion will affect the crack growth. The dislocations which are segregated with C require an extra force in order to be released for slip [66,67]. According to Cottrell *et al.* [66], the critical tensile stress required to release the C-segregated dislocation for plastic slip depends on the interaction energy of the C atoms (especially the central row of C atoms within the dislocation core) with the dislocation [66]. Using the classical approach of Cottrell *et al.* [66], the presence of a Cottrell atmosphere at the dislocations can lead to an approximate increase of 25 % in the yield strength of the steels. It should be noted that this increase in the yield strength is a rough estimation as it is challenging to accurately estimate the interaction energy of the dislocation and the C atoms at the dislocation center line. Aforementioned increase in the yield strength due to C-segregated dislocations will lead to the

retardation of the FCGR according to Eq. 8. Thus, such C-segregated dislocations when lying in the vicinity of the crack in the WEL, will contribute to an increase in their fracture toughness.

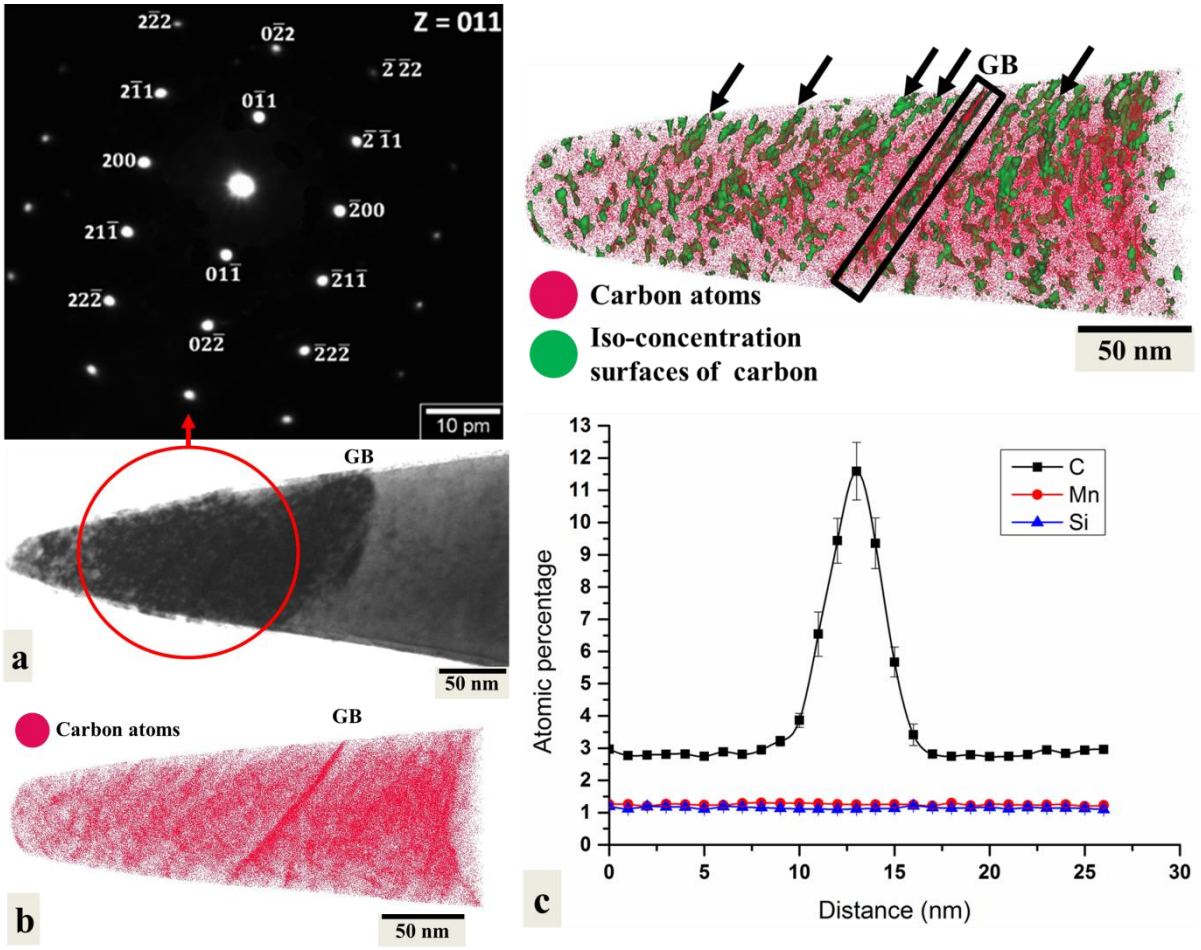

Fig. 7. Correlative TEM and APT measurements from the WEL at 10 μm below rail surface: (a) Bright field TEM image of APT tip showing a grain boundary and a selected area diffraction pattern from the encircled region, (b) APT measurement of the same tip showing C segregation at the Grain Boundary (GB), (c) C atom map overlapped with 7 at.% C iso-concentration surfaces (in green) showing regions of high C concentrations at dislocations (indicated by arrows). One dimensional concentration profile (taken perpendicular to the GB) shows the GB segregation.

4. Conclusions

The WELs formed in the pearlitic microstructure of rail steels are considered as one of the reasons for micro-cracking in rails. These micro-cracks grow inside the rail and cause failure. The current study shows the first quantification of WEL fracture toughness and its correlation

to the WEL microstructure. Results from the current study are of importance for modelling and understanding of wheel-rail contact in the presence of the WELs. The results from WEL models can be used to estimate the critical WEL thickness for preventive maintenance to ensure safety and help minimizing grinding costs. Following conclusions are drawn based on the current investigation:

1. WELs show elastic-plastic and semi-brittle fracture during the micromechanical *in situ* fracture experiments and the fracture toughness is 21.5 ± 3 MPa√m to 25.4 ± 2.3 MPa√m. WELs also show crack branching, crack blunting and micro-dimples at the fracture surface which validate the categorization as semi-brittle failure.
2. Based on a comparison of the fracture toughness and critical defect size of WELs with the undeformed pearlitic steels, WELs are detrimental for rails.
3. We observed a high GND density, ultrafine grain size and high C concentrations in the martensitic matrix of the WEL which leads to high hardness values in the WELs.
4. In contrast to the comparison with the cold drawn pearlitic wires, the plasticity and semi-brittle fracture in the WEL is attributed to its larger grain size, presence of retained austenite and strain-induced austenite to martensitic transformation during the crack growth.
5. Large martensite grains with low GND density are observed in the WEL which contribute to the increase in plasticity due to high dislocation mobility in these grains ahead the crack. This is also one of the reasons for the semi-brittle fracture of the WEL.
6. We observed the C segregation at the grain boundaries in the WELs which promotes the grain boundary cohension and softens the martensitic matrix by lowering the C concentration. Thus, this C redistribution is one of the reasons for semi-brittle fracture and higher fracture toughness of the WELs than the quenched martesnite.
7. The C segregation at the dislocations was observed in the WEL using APT which will affect the crack propagation and contribute to increase the fracture toughness as such dislocations in the vicinity of the crack require extra force to be released for slip.

Acknowledgements

This research was carried out under project number F91.10.12475b in the framework of the Partnership Program of the Materials innovation institute M2i (www.m2i.nl) and the Foundation for Fundamental Research on Matter (FOM) (www.fom.nl), which is part of the

Netherlands Organisation for Scientific Research (www.nwo.nl). We would like to express our gratitude to Dr. Stefan Zaefferer and Mrs. Monika Nellessen for providing assistance during the EBSD measurement on the microcantilevers. We thank Mr. Viswanadh Gowtham Arigela for his support during this research. We also would like to thank ProRail for providing the financial support and the specimens for this research. M. Herbig acknowledges funding by the German Federal Ministry of Education and Research (BMBF) through grant 03SF0535.

References

[1] Wikipedia contributors, List of countries by rail transport network size, (2017). https://en.wikipedia.org/wiki/List_of_countries_by_rail_transport_network_size.

[2] D. Nikas, K.A. Meyer, J. Ahlström, Characterization of deformed pearlitic rail steel, IOP Conf. Ser. Mater. Sci. Eng. 219 (2017) 12035. doi:10.1088/1757-899x/219/1/012035.

[3] J. Takahashi, K. Kawakami, M. Ueda, Atom probe tomography analysis of the white etching layer in a rail track surface, Acta Mater. 58 (2010) 3602–3612. doi:10.1016/J.ACTAMAT.2010.02.030.

[4] M. Steenbergen, R. Dollevoet, On the mechanism of squat formation on train rails – Part I: Origination, Int. J. Fatigue. 47 (2013) 361–372. doi:10.1016/J.IJFATIGUE.2012.04.023.

[5] J. Wu, R.H. Petrov, M. Naeimi, Z. Li, R. Dollevoet, J. Sietsma, Laboratory simulation of martensite formation of white etching layer in rail steel, Int. J. Fatigue. 91 (2016) 11–20. doi:10.1016/J.IJFATIGUE.2016.05.016.

[6] J. Wu, R.H. Petrov, S. Li, Z. Li, S. Godet, L. Malet, J. Sietsma, Characterization of structural change in rail surface using advanced automatic crystallographic orientation microscopy, in: COMPRAIL2016, WIT Press, 2016: pp. 367–376. doi:10.2495/CR160331.

[7] J. Wu, R.H. Petrov, S. Kölling, P. Koenraad, L. Malet, S. Godet, J. Sietsma, Micro and Nanoscale Characterization of Complex Multilayer-Structured White Etching Layer in Rails, Met. . 8 (2018). doi:10.3390/met8100749.

[8] F.C. Zhang, B. Lv, C.L. Zheng, Q. Zou, M. Zhang, M. Li, T.S. Wang, Microstructure of the worn surfaces of a bainitic steel railway crossing, Wear. 268 (2010) 1243–1249. doi:10.1016/J.WEAR.2010.01.016.

[9] W. Österle, H. Rooch, A. Pyzalla, L. Wang, Investigation of white etching layers on rails by optical microscopy, electron microscopy, X-ray and synchrotron X-ray diffraction, Mater. Sci. Eng. A. 303 (2001) 150–157. doi:10.1016/S0921-5093(00)01842-6.

[10] S.B. Newcomb, W.M. Stobbs, A transmission electron microscopy study of the white-etching layer on a rail head, Mater. Sci. Eng. 66 (1984) 195–204. doi:10.1016/0025-

5416(84)90180-0.

[11] W. Lojkowski, M. Djahanbakhsh, G. Bürkle, S. Gierlotka, W. Zielinski, H.-J. Fecht, Nanostructure formation on the surface of railway tracks, Mater. Sci. Eng. A. 303 (2001) 197–208. doi:10.1016/S0921-5093(00)01947-X.

[12] M. Steenbergen, R. Dollevoet, On the mechanism of squat formation on train rails – Part II: Growth, Int. J. Fatigue. 47 (2013) 373–381. doi:10.1016/J.IJFATIGUE.2012.04.019.

[13] G. Baumann, H.J. Fecht, S. Liebelt, Formation of white-etching layers on rail treads, Wear. 191 (1996) 133–140. doi:10.1016/0043-1648(95)06733-7.

[14] A. Pyzalla, L. Wang, E. Wild, T. Wroblewski, Changes in microstructure, texture and residual stresses on the surface of a rail resulting from friction and wear, Wear. 251 (2001) 901–907. doi:10.1016/S0043-1648(01)00748-7.

[15] A.P. Patra, P. Söderholm, U. Kumar, Uncertainty estimation in railway track life-cycle cost: a case study from Swedish National Rail Administration, Proc. Inst. Mech. Eng. Part F J. Rail Rapid Transit. 223 (2008) 285–293. doi:10.1243/09544097JRRT235.

[16] P. Sroba, M. Roney, Rail grinding best practices, in: Proc. AREMA Annu. Conf. Chicago, 2003.

[17] H.W. Zhang, S. Ohsaki, S. Mitao, M. Ohnuma, K. Hono, Microstructural investigation of white etching layer on pearlite steel rail, Mater. Sci. Eng. A. 421 (2006) 191–199. doi:10.1016/J.MSEA.2006.01.033.

[18] L. Wang, A. Pyzalla, W. Stadlbauer, E.. Werner, Microstructure features on rolling surfaces of railway rails subjected to heavy loading, Mater. Sci. Eng. A. 359 (2003) 31–43. doi:10.1016/S0921-5093(03)00327-7.

[19] A. Kumar, G. Agarwal, R. Petrov, S. Goto, J. Sietsma, M. Herbig, Microstructural evolution of white and brown etching layers in pearlitic rail steels, Acta Mater. 171 (2019) 48–64. doi:https://doi.org/10.1016/j.actamat.2019.04.012.

[20] A. Al-Juboori, H. Zhu, D. Wexler, H. Li, C. Lu, A. McCusker, J. McLeod, S. Pannila, J. Barnes, Evolution of rail surface degradation in the tunnel: The role of water on squat growth under service conditions, Eng. Fract. Mech. 209 (2019) 32–47. doi:10.1016/J.ENGFRACMECH.2019.01.018.

[21] B.N. Jaya, J.M. Wheeler, J. Wehrs, J.P. Best, R. Soler, J. Michler, C. Kirchlechner, G. Dehm, Microscale Fracture Behavior of Single Crystal Silicon Beams at Elevated Temperatures, Nano Lett. 16 (2016) 7597–7603. doi:10.1021/acs.nanolett.6b03461.

[22] D.E.J. Armstrong, M.E. Rogers, S.G. Roberts, Micromechanical testing of stress corrosion cracking of individual grain boundaries, Scr. Mater. 61 (2009) 741–743. doi:10.1016/J.SCRIPTAMAT.2009.06.017.

[23] D.E.J. Armstrong, A.J. Wilkinson, S.G. Roberts, Micro-mechanical measurements of fracture toughness of bismuth embrittled copper grain boundaries, Philos. Mag. Lett. 91 (2011) 394–400. doi:10.1080/09500839.2011.573813.

[24] H. Chan, S.G. Roberts, J. Gong, Micro-scale fracture experiments on zirconium

hydrides and phase boundaries, J. Nucl. Mater. 475 (2016) 105–112. doi:10.1016/J.JNUCMAT.2016.03.026.

[25] A. Stratulat, D.E.J. Armstrong, S.G. Roberts, Micro-mechanical measurement of fracture behaviour of individual grain boundaries in Ni alloy 600 exposed to a pressurized water reactor environment, Corros. Sci. 104 (2016) 9–16. doi:10.1016/J.CORSCI.2015.10.019.

[26] Y. Zou, P. Okle, H. Yu, T. Sumigawa, T. Kitamura, S. Maiti, W. Steurer, R. Spolenak, Fracture properties of a refractory high-entropy alloy: In situ micro-cantilever and atom probe tomography studies, Scr. Mater. 128 (2017) 95–99. doi:10.1016/J.SCRIPTAMAT.2016.09.036.

[27] D. Di Maio, S.G. Roberts, Measuring fracture toughness of coatings using focused-ion-beam-machined microbeams, J. Mater. Res. 20 (2005) 299–302.

[28] K. Matoy, H. Schönherr, T. Detzel, T. Schöberl, R. Pippan, C. Motz, G. Dehm, A comparative micro-cantilever study of the mechanical behavior of silicon based passivation films, Thin Solid Films. 518 (2009) 247–256. doi:10.1016/J.TSF.2009.07.143.

[29] A. Hohenwarter, B. Völker, M.W. Kapp, Y. Li, S. Goto, D. Raabe, R. Pippan, Ultra-strong and damage tolerant metallic bulk materials: A lesson from nanostructured pearlitic steel wires, Sci. Rep. 6 (2016) 33228. https://doi.org/10.1038/srep33228.

[30] V. Schnabel, B.N. Jaya, M. Köhler, D. Music, C. Kirchlechner, G. Dehm, D. Raabe, J.M. Schneider, Electronic hybridisation implications for the damage-tolerance of thin film metallic glasses, Sci. Rep. 6 (2016) 36556. https://doi.org/10.1038/srep36556.

[31] T.P. HALFORD, K. TAKASHIMA, Y. HIGO, P. BOWEN, Fracture tests of microsized TiAl specimens, Fatigue Fract. Eng. Mater. Struct. 28 (2005) 695–701. doi:10.1111/j.1460-2695.2005.00893.x.

[32] S. Massl, W. Thomma, J. Keckes, R. Pippan, Investigation of fracture properties of magnetron-sputtered TiN films by means of a FIB-based cantilever bending technique, Acta Mater. 57 (2009) 1768–1776. doi:10.1016/J.ACTAMAT.2008.12.018.

[33] S. Wurster, C. Motz, R. Pippan, Characterization of the fracture toughness of micro-sized tungsten single crystal notched specimens, Philos. Mag. 92 (2012) 1803–1825. doi:10.1080/14786435.2012.658449.

[34] J. Ast, B. Merle, K. Durst, M. Göken, Fracture toughness evaluation of NiAl single crystals by microcantilevers—a new continuous J-integral method, J. Mater. Res. 31 (2016) 3786–3794.

[35] M. Herbig, P. Choi, D. Raabe, Combining structural and chemical information at the nanometer scale by correlative transmission electron microscopy and atom probe tomography, Ultramicroscopy. 153 (2015) 32–39. doi:10.1016/J.ULTRAMIC.2015.02.003.

[36] M. Herbig, D. Raabe, Y.J. Li, P. Choi, S. Zaefferer, S. Goto, Atomic-Scale Quantification of Grain Boundary Segregation in Nanocrystalline Material, Phys. Rev. Lett. 112 (2014) 126103. doi:10.1103/PhysRevLett.112.126103.

[37] M. Herbig, Spatially correlated electron microscopy and atom probe tomography: Current possibilities and future perspectives, Scr. Mater. 148 (2018) 98–105. doi:10.1016/J.SCRIPTAMAT.2017.03.017.

[38] S.K. Makineni, M. Lenz, P. Kontis, Z. Li, A. Kumar, P.J. Felfer, S. Neumeier, M. Herbig, E. Spiecker, D. Raabe, B. Gault, Correlative Microscopy—Novel Methods and Their Applications to Explore 3D Chemistry and Structure of Nanoscale Lattice Defects: A Case Study in Superalloys, JOM. 70 (2018). doi:10.1007/s11837-018-2802-7.

[39] S.K. Makineni, A. Kumar, M. Lenz, P. Kontis, T. Meiners, C. Zenk, S. Zaefferer, G. Eggeler, S. Neumeier, E. Spiecker, D. Raabe, B. Gault, On the diffusive phase transformation mechanism assisted by extended dislocations during creep of a single crystal CoNi-based superalloy, Acta Mater. 155 (2018). doi:10.1016/j.actamat.2018.05.074.

[40] W. Lu, M. Herbig, C.H. Liebscher, L. Morsdorf, R.K.W. Marceau, G. Dehm, D. Raabe, Formation of eta carbide in ferrous martensite by room temperature aging, Acta Mater. 158 (2018) 297–312. doi:10.1016/J.ACTAMAT.2018.07.071.

[41] S. Suresh, Micromechanisms of fatigue crack growth retardation following overloads, Eng. Fract. Mech. 18 (1983) 577–593. doi:10.1016/0013-7944(83)90051-6.

[42] H. A., P. R., Fracture and fracture toughness of nanopolycrystalline metals produced by severe plastic deformation, Philos. Trans. R. Soc. A Math. Phys. Eng. Sci. 373 (2015) 20140366. doi:10.1098/rsta.2014.0366.

[43] A. K. Saxena, A. Kumar, S. Brinckmann, M. Herbig, G. Dehm, C. Kirchlechner, Micro fracture investigations of white etching layers, Mater. Des. 180 (2019) 107892. doi:https://doi.org/10.1016/j.matdes.2019.107892.

[44] A. Hohenwarter, A. Taylor, R. Stock, R. Pippan, Effect of Large Shear Deformations on the Fracture Behavior of a Fully Pearlitic Steel, Metall. Mater. Trans. A. 42 (2011) 1609–1618. doi:10.1007/s11661-010-0541-7.

[45] B.N. Jaya, S. Goto, G. Richter, C. Kirchlechner, G. Dehm, Fracture behavior of nanostructured heavily cold drawn pearlitic steel wires before and after annealing, Mater. Sci. Eng. A. 707 (2017) 164–171. doi:10.1016/J.MSEA.2017.09.010.

[46] A. Kumar, A. Dutta, S.K. Makineni, M. Herbig, R.H. Petrov, J. Sietsma, In-situ observation of strain partitioning and damage development in continuously cooled carbide-free bainitic steels using micro digital image correlation, Mater. Sci. Eng. A. 757 (2019) 107–116. doi:10.1016/J.MSEA.2019.04.098.

[47] R. Pippan, S. Wurster, D. Kiener, Fracture mechanics of micro samples: Fundamental considerations, Mater. Des. 159 (2018) 252–267. doi:https://doi.org/10.1016/j.matdes.2018.09.004.

[48] S. Djaziri, Y. Li, G.A. Nematollahi, B. Grabowski, S. Goto, C. Kirchlechner, A. Kostka, S. Doyle, J. Neugebauer, D. Raabe, Deformation-Induced Martensite: A New Paradigm for Exceptional Steels, Adv. Mater. 28 (2016) 7753–7757.

[49] A. Kumar, S.K. Makineni, A. Dutta, C. Goulas, M. Steenbergen, R.H. Petrov, J. Sietsma, Design of high-strength and damage-resistant carbide-free fine bainitic steels

for railway crossing applications, Mater. Sci. Eng. A. 759 (2019) 210–223. doi:10.1016/J.MSEA.2019.05.043.

[50] G. Krauss, Martensite in steel: strength and structure, Mater. Sci. Eng. A. 273–275 (1999) 40–57. doi:https://doi.org/10.1016/S0921-5093(99)00288-9.

[51] R. Pippan, A. Hohenwarter, The importance of fracture toughness in ultrafine and nanocrystalline bulk materials, Mater. Res. Lett. 4 (2016) 127–136.

[52] Q. Liu, D. Juul Jensen, N. Hansen, Effect of grain orientation on deformation structure in cold-rolled polycrystalline aluminium, Acta Mater. 46 (1998) 5819–5838. doi:10.1016/S1359-6454(98)00229-8.

[53] H. Li, M. Koyama, T. Sawaguchi, K. Tsuzaki, H. Noguchi, Importance of crack-propagation-induced ε-martensite in strain-controlled low-cycle fatigue of high-Mn austenitic steel, Philos. Mag. Lett. 95 (2015) 303–311. doi:10.1080/09500839.2015.1052029.

[54] A.G. Pineau, R.M. Pelloux, Influence of strain-induced martensitic transformations on fatigue crack growth rates in stainless steels, Metall. Trans. 5 (1974) 1103–1112. doi:10.1007/BF02644322.

[55] E. Hornbogen, Martensitic transformation at a propagating crack, Acta Metall. 26 (1978) 147–152. doi:https://doi.org/10.1016/0001-6160(78)90211-0.

[56] J.M. Moyer, G.S. Ansell, The volume expansion accompanying the martensite transformation in iron-carbon alloys, Metall. Trans. A. 6 (1975) 1785. doi:10.1007/BF02642308.

[57] W.-L. Li, J.C.M. Li, The effect of grain size on fracture toughness, Philos. Mag. A. 59 (1989) 1245–1261. doi:10.1080/01418618908221173.

[58] X. Zhang, N. Hansen, A. Godfrey, X. Huang, Dislocation-based plasticity and strengthening mechanisms in sub-20 nm lamellar structures in pearlitic steel wire, Acta Mater. 114 (2016) 176–183. doi:10.1016/J.ACTAMAT.2016.04.040.

[59] Y.J. Li, P. Choi, S. Goto, C. Borchers, D. Raabe, R. Kirchheim, Evolution of strength and microstructure during annealing of heavily cold-drawn 6.3 GPa hypereutectoid pearlitic steel wire, Acta Mater. 60 (2012) 4005–4016. doi:10.1016/J.ACTAMAT.2012.03.006.

[60] Y.J. Li, P. Choi, C. Borchers, S. Westerkamp, S. Goto, D. Raabe, R. Kirchheim, Atomic-scale mechanisms of deformation-induced cementite decomposition in pearlite, Acta Mater. 59 (2011) 3965–3977. doi:10.1016/J.ACTAMAT.2011.03.022.

[61] Y. Li, D. Raabe, M. Herbig, P.-P. Choi, S. Goto, A. Kostka, H. Yarita, C. Borchers, R. Kirchheim, Segregation Stabilizes Nanocrystalline Bulk Steel with Near Theoretical Strength, Phys. Rev. Lett. 113 (2014) 106104. doi:10.1103/PhysRevLett.113.106104.

[62] R.P. Messmer, C.L. Briant, The role of chemical bonding in grain boundary embrittlement, Acta Metall. 30 (1982) 457–467.

[63] D. Raabe, M. Herbig, S. Sandlöbes, Y. Li, D. Tytko, M. Kuzmina, D. Ponge, P.-P. Choi, Grain boundary segregation engineering in metallic alloys: A pathway to the

design of interfaces, Curr. Opin. Solid State Mater. Sci. 18 (2014) 253–261. doi:10.1016/J.COSSMS.2014.06.002.

[64] R. Wu, A.J. Freeman, G.B. Olson, Effects of carbon on Fe-grain-boundary cohesion: First-principles determination, Phys. Rev. B. 53 (1996) 7504.

[65] J. Takahashi, M. Kosaka, K. Kawakami, T. Tarui, Change in carbon state by low-temperature aging in heavily drawn pearlitic steel wires, Acta Mater. 60 (2012) 387–395. doi:10.1016/J.ACTAMAT.2011.09.014.

[66] A.H. Cottrell, B.A. Bilby, Dislocation theory of yielding and strain ageing of iron, Proc. Phys. Soc. Sect. A. 62 (1949) 49.

[67] M. Calcagnotto, Y. Adachi, D. Ponge, D. Raabe, Deformation and fracture mechanisms in fine- and ultrafine-grained ferrite/martensite dual-phase steels and the effect of aging, Acta Mater. 59 (2011) 658–670. doi:10.1016/J.ACTAMAT.2010.10.002.

Supplementary Material_video

Click here to download Supplementary Material: Microcantilever_1.avi

Supplementary Material_1

Click here to download Supplementary Material: Supplementary Material.docx

*Graphical Abstract

Fracture behaviour of white etching layers